

Impact of interstitial C on phase stability and stacking-fault energy of the CrMnFeCoNi high-entropy alloy

Ikeda, Yuji; Tanaka, Isao; Neugebauer, Jörg; Körmann, Fritz

DOI

[10.1103/PhysRevMaterials.3.113603](https://doi.org/10.1103/PhysRevMaterials.3.113603)

Publication date

2019

Document Version

Final published version

Published in

Physical Review Materials

Citation (APA)

Ikeda, Y., Tanaka, I., Neugebauer, J., & Körmann, F. (2019). Impact of interstitial C on phase stability and stacking-fault energy of the CrMnFeCoNi high-entropy alloy. *Physical Review Materials*, 3(11), Article 113603. <https://doi.org/10.1103/PhysRevMaterials.3.113603>

Important note

To cite this publication, please use the final published version (if applicable). Please check the document version above.

Copyright

Other than for strictly personal use, it is not permitted to download, forward or distribute the text or part of it, without the consent of the author(s) and/or copyright holder(s), unless the work is under an open content license such as Creative Commons.

Takedown policy

Please contact us and provide details if you believe this document breaches copyrights. We will remove access to the work immediately and investigate your claim.

Impact of interstitial C on phase stability and stacking-fault energy of the CrMnFeCoNi high-entropy alloy

Yuji Ikeda ^{1,2,*}, Isao Tanaka ^{2,3,4,5}, Jörg Neugebauer ¹ and Fritz Körmann ^{1,6}

¹Computational Materials Design, Max-Planck-Institut für Eisenforschung GmbH, 40237 Düsseldorf, Germany

²Department of Materials Science and Engineering, Kyoto University, Kyoto 606-8501, Japan

³Center for Elements Strategy Initiative for Structural Materials, Kyoto University, Kyoto 606-8501, Japan

⁴Center for Materials Research by Information Integration, National Institute for Materials Science, Tsukuba 305-0047, Japan

⁵Nanostructures Research Laboratory, Japan Fine Ceramics Center, Nagoya 456-8587, Japan

⁶Materials Science and Engineering, Delft University of Technology, 2628 CD Delft, The Netherlands



(Received 5 July 2019; published 12 November 2019)

Interstitial alloying in CrMnFeCoNi-based high-entropy alloys is known to modify their mechanical properties. Specifically, strength can be increased due to interstitial solid-solution hardening, while simultaneously affecting ductility. In this paper, first-principles calculations are carried out to analyze the impact of interstitial C atoms on CrMnFeCoNi in the fcc and the hcp phases. Our results show that C solution energies are widely spread and sensitively depend on the specific local environments. Using the computed solution-energy distributions together with statistical mechanics concepts, we determine the impact of C on the phase stability. C atoms are found to stabilize the fcc phase as compared to the hcp phase, indicating that the stacking-fault energy of CrMnFeCoNi increases due to C alloying. Using our extensive set of first-principles computed solution energies, correlations between them and local environments around the C atoms are investigated. This analysis reveals, e.g., that the local valence-electron concentration around a C atom is well correlated with its solution energy.

DOI: [10.1103/PhysRevMaterials.3.113603](https://doi.org/10.1103/PhysRevMaterials.3.113603)

I. INTRODUCTION

High-entropy alloys (HEAs) or complex concentrated alloys based on $3d$ transition metals have attracted enormous attention, particularly due to their outstanding mechanical properties. The equiatomic CrMnFeCoNi alloy, also termed as the Cantor alloy [1], shows a remarkable combination of strength and ductility [2–5]. Their impressive mechanical properties could be further enhanced by modifying the compositions away from equiatomic CrMnFeCoNi [6–19].

Another promising direction to further improve the mechanical properties of HEAs is interstitial alloying, e.g., with C. The impact of interstitial C atoms in HEAs has been investigated in several previous experimental studies [10,16,18,20–27]. In equiatomic CrMnFeCoNi, the addition of C atoms is known to increase the yield and the ultimate strengths [18,20,24] while also impacting ductility. Enhanced yield and ultimate strengths are also found for interstitial-alloyed $\text{Cr}_{0.1}\text{Mn}_{0.3}\text{Fe}_{0.5}\text{Co}_{0.1}$ [10] and $\text{Cr}_{0.1}\text{Mn}_{0.4}\text{Fe}_{0.4}\text{Co}_{0.1}$ [25] without critical reduction of ductility. To fine tune the mechanical properties by interstitial alloying, an understanding of the fundamental mechanisms on the atomic scale is required. Particularly for HEAs, each interstitial site displays a different local environment and thus a specific solution energy. Resolving such complex dependencies is intractably hard by experiments alone.

To study the impact of interstitial C alloying from an atomistic viewpoint in detail, first-principles calculation is an accurate and efficient approach. A number of first-principles studies have been reported for the impact of C atoms in traditional $3d$ transition metals and alloys like Fe [28–46], Ni [40,47–52], Fe–Cr–Ni stainless steels [40,45], and high-Mn steels [37,53–62]. For CrMnFeCoNi-based HEAs, however, studies on the impact of interstitial C alloying based on first-principles calculations are still lacking.

In the present paper, we investigate the impact of interstitial C atoms on the equiatomic CrMnFeCoNi HEA based on first-principles calculations. Both the face-centered cubic (fcc) and the hexagonal close-packed (hcp) phases of CrMnFeCoNi are modeled based on the supercell approach to evaluate stacking-fault energies (SFEs). The solution energies of interstitial C atoms are computed for both phases. A large number of interstitial sites are investigated to elucidate the dependence on the local environments around C atoms.

II. COMPUTATIONAL DETAILS

A. Stacking-fault energy

The SFEs of fcc austenitic steels, particularly of high-Mn steels, have empirically been known to correlate with their deformation behaviors [63–67]. Also for $3d$ -transition-element-based HEAs, their SFEs have also been measured in experiments [8,17,26,68–71] and computed based on first-principles simulations [72–84]. While the impact of C atoms on the SFEs of HEAs has also been discussed in experimental

*y.ikeda@mpie.de

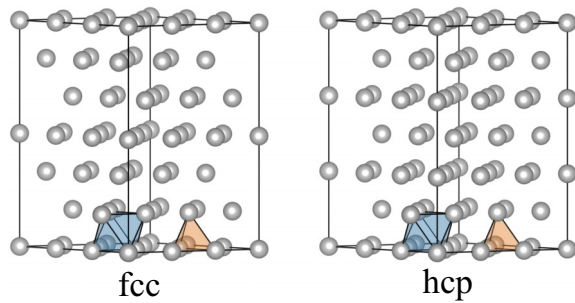


FIG. 1. Simulation cells with 54 atoms for the fcc and the hcp phases in the present paper. The blue and the orange regions indicate octahedral and tetrahedral sites, respectively. Visualization is performed using the VESTA code [86].

studies [10,16,18,20,21,25,26], this has, to the best of our knowledge, not yet been intensively investigated based on first-principles simulations.

In the present paper, the SFE of fcc CrMnFeCoNi was computed based on the first-order axial Ising model (AIM1) [85] as

$$\gamma_{\text{SF}} \approx \frac{2(F^{\text{hcp}} - F^{\text{fcc}})}{NA}, \quad (1)$$

where F^α denotes the Helmholtz energy per simulation cell of the phase α , A denotes the area of one close-packing layer in the simulation cell, and N denotes the number of close-packing layers in the simulation cell. This approximation may be intuitively understood because the fcc stacking faults locally have the same layer stacking as the hcp phase.

B. Models without interstitial atoms

The CrMnFeCoNi HEA was modeled based on the supercell approach. Both the fcc and the hcp phases were investigated to compute the SFE (see Sec. II A for details). To improve the computational accuracy, 54-atom fcc and hcp supercells are modeled with identical simulation-cell shapes as shown in Fig. 1. The fcc unit cell has the $\langle 111 \rangle$ direction as the third axis and displays the “ABCABC” stacking of the close-packed $\{111\}$ layers, while the hcp unit cell has the “ABABAB” stacking of the close-packed $\{0001\}$ layers. These supercells have six layers, and each layer consists of nine atoms. Ideal mixing of the elements in CrMnFeCoNi was approximated based on special quasirandom structures (SQSs) [87]. The first and the second nearest-neighbor pairs are optimized to be close to the ideal mixing state. We constructed a single five-component SQS configuration for each of the fcc and the hcp phases. Based on this construction, $5! = 120$ supercell models were obtained for each SQS by permuting the order of the five elements. Note that the 54-atom SQSs have a composition ratio of 11 : 11 : 11 : 11 : 10, which slightly deviates from the equiatomic, and hence the energies of equiatomic CrMnFeCoNi were evaluated by taking the average over the 120 supercell models.

C. Solution energies of interstitial atoms

The energy gained by placing C atoms in the CrMnFeCoNi alloy modifies thermodynamic quantities such as SFEs. To

compute solution energies, both octahedral and tetrahedral sites, surrounded by six and four atoms in the first nearest-neighbor (1NN) shell, respectively, were considered as potential interstitial sites. Note that the octahedral and the tetrahedral sites in the fcc phase are geometrically very similar to those in the hcp phases, as also visualized in Fig. 1. The solution energies ΔE_{sol} of C atoms were computed as

$$\Delta E_{\text{sol}} = E(\text{alloy} + \text{C}) - [E(\text{alloy}) + E(\text{C})], \quad (2)$$

where $E(\text{alloy} + \text{C})$ and $E(\text{alloy})$ are the energies of the alloys per simulation cell with and without one C atom, respectively, and $E(\text{C})$ is the energy of graphite per atom. In the generalized gradient approximation (GGA), the determination of the total energy of graphite is limited due to the inadequate description of the van der Waals interactions resulting, e.g., in a large overestimation of the energy difference between graphite and diamond [30,35,38,88]. In experiments, the graphite enthalpy is 0.019 eV/atom lower than the diamond enthalpy at standard conditions [89]. We therefore obtained the graphite energy by computing the diamond energy and then shifting it by the above empirically known enthalpy difference.

Unlike pure metals and ordered alloys, interstitial sites in disordered alloys have different local environments from each other and thus different solution energies specific to the corresponding local environments (see Sec. II E for details). The solution energies in such disordered alloys are therefore described as the density of states (DOS). In the present paper, the solution-energy DOS $n(\epsilon)$, where $\epsilon = \Delta E_{\text{sol}}$, is normalized as

$$\int_{-\infty}^{\infty} n(\epsilon) d\epsilon = 1. \quad (3)$$

Under the AIM1 [Eq. (1)], the impact of an interstitial atom in the simulation cell on the SFE is computed as

$$\Delta \gamma_{\text{SF}} \approx \frac{2(\Delta F_{\text{sol}}^{\text{hcp}} - \Delta F_{\text{sol}}^{\text{fcc}})}{NA}, \quad (4)$$

where $\Delta F_{\text{sol}}^\alpha$ is the contribution of one interstitial atom to the Helmholtz energy for the phase α . In general, $\Delta F_{\text{sol}} = \Delta F_{\text{sol}}(T, x)$ depends on temperature, T , and the ratio of interstitial atoms to available interstitial sites, x , and can be separated as

$$\Delta F_{\text{sol}}(T, x) = \Delta U_{\text{sol}}(T, x) - T \Delta S_{\text{sol}}(T, x), \quad (5)$$

where $\Delta U_{\text{sol}}(T, x)$ and $\Delta S_{\text{sol}}(T, x)$ are the contributions of the interstitial atom to the internal energy and to the entropy, respectively. Note that in Eq. (4) x must be the same between the fcc and the hcp phases, which corresponds to the same concentrations of the interstitial element in the bulk region and on stacking faults (see Sec. II D for segregation of interstitial atoms).

To compute ΔF_{sol} , the following two thermodynamic limits were considered. In the first scenario, interstitial atoms are assumed to occupy the interstitial sites fully randomly irrespective of their solution energies ΔE_{sol} . This could be, e.g., realized by rapid quenching from high temperatures in which the C atoms are “frozen” in their randomly distributed high-temperature state. We therefore refer to this scenario as the *ideal quenched condition*. In the second scenario, interstitial atoms are assumed to occupy the interstitial sites according

to the canonical ensemble for ΔE_{sol} . This corresponds to the situation in which the disordered alloy is annealed for a sufficiently long time and hence the C atoms can diffuse into the thermodynamically favorable interstitial sites at a given temperature. We refer to this scenario hereafter as the *ideal annealed condition*. In both the conditions, it is assumed that one interstitial site can be occupied by at most one interstitial atom and that there are no interactions between the interstitial atoms (the dilute limit approximation) [90].

In the ideal quenched condition, $\Delta U_{\text{sol}}(T, x)$ is simply given as the average solution energy $\overline{\Delta E}_{\text{sol}}$ over all interstitial sites:

$$\Delta U_{\text{sol}}(T, x) = \int_{-\infty}^{\infty} n(\epsilon) \epsilon d\epsilon = \overline{\Delta E}_{\text{sol}}, \quad (6)$$

which is actually independent of T and x , and $\Delta S_{\text{sol}}(T, x)$ equals to zero because each interstitial atom is now assumed to be pinned to a certain interstitial site. Thus, $\Delta F_{\text{sol}}(T, x)$ in the ideal quenched condition is given as

$$\Delta F_{\text{sol}} = \overline{\Delta E}_{\text{sol}}. \quad (7)$$

In the ideal annealed condition, an interstitial site is occupied with the probability given by the Fermi-Dirac distribution

$$f(\epsilon; T, \mu) = \left[\exp\left(\frac{\epsilon - \mu}{k_B T}\right) + 1 \right]^{-1}, \quad (8)$$

where k_B is the Boltzmann constant. The chemical potential $\mu = \mu(T, x)$ of the interstitial element in the alloy is determined for given T and x to satisfy

$$\int_{-\infty}^{\infty} n(\epsilon) f(\epsilon; T, \mu) d\epsilon = x. \quad (9)$$

Once $\mu(T, x)$ is self-consistently determined from Eqs. (8) and (9), $\Delta U_{\text{sol}}(T, x)$ and $\Delta S_{\text{sol}}(T, x)$ are computed as

$$\Delta U_{\text{sol}}(T, x) = \frac{1}{x} \int_{-\infty}^{\infty} n(\epsilon) f(\epsilon; T, \mu) \epsilon d\epsilon, \quad (10)$$

$$\Delta S_{\text{sol}}(T, x) = \frac{k_B}{x} \int_{-\infty}^{\infty} n(\epsilon) s(\epsilon; T, \mu) d\epsilon, \quad (11)$$

$$s(\epsilon; T, \mu) = -[f \ln f + (1 - f) \ln(1 - f)], \quad (12)$$

where $f = f(\epsilon; T, \mu)$ [91].

At the high-temperature limit ($T \rightarrow \infty$) in the ideal annealed condition, all the available interstitial sites can be occupied fully randomly irrespective of the solution energies, like in the ideal quenched condition. The $\Delta U_{\text{sol}}(T, x)$ and the $\Delta S_{\text{sol}}(T, x)$ at the high-temperature limit can therefore be obtained by replacing $f = f(\epsilon; T, x)$ with x in Eqs. (10)–(12). At the high-concentration limit ($x = 1$) in the ideal annealed condition, all the available interstitial sites are occupied by the interstitial atoms, and therefore $\Delta U_{\text{sol}}(T, x)$ and $\Delta S_{\text{sol}}(T, x)$ are obtained by, again, replacing $f = f(\epsilon; T, x)$ with $x = 1$ in Eqs. (10)–(12). In both the limits, $\Delta U_{\text{sol}}(T, x)$ becomes equal to $\overline{\Delta E}_{\text{sol}}$, and $\Delta S_{\text{sol}}(T, x)$ becomes a constant independent of the focused phases. Thus, at the high-temperature or the high-concentration limit, the difference of ΔF_{sol} between the fcc and the hcp phases ($\Delta F_{\text{sol}}^{\text{hcp}} - \Delta F_{\text{sol}}^{\text{fcc}}$) in the ideal annealed condition equals to that in the ideal quenched condition.

In the dilute limit, where interactions between interstitial atoms can be neglected, the impact of an interstitial atom is

proportional to x , i.e., the ratio of interstitial atoms to available interstitial sites. The contributions of 1 wt. % and 1 at. % interstitial C atoms to the SFE were computed in the dilute limit, i.e., by linear scaling of the contribution of the results obtained for one C atom in a 54-atom simulation cell.

D. Segregation of interstitial atoms at stacking faults

Suppose that there coexist multiple phases in a disordered alloy satisfying

$$\sum_{\alpha} y^{\alpha} = 1, \quad (13)$$

where y^{α} denotes the atomic fraction of the phase α . When interstitial atoms are distributed among the multiple phases according to the canonical ensemble, these multiple phases share the same chemical potential of the interstitial element in the alloy. This chemical potential $\mu = \mu(T, x)$ is self-consistently determined based on Eqs. (8) and (9) by the solution-energy DOS $n(\epsilon)$ for the whole alloy obtained as

$$n(\epsilon) = \sum_{\alpha} y^{\alpha} n^{\alpha}(\epsilon), \quad (14)$$

where $\epsilon (= \Delta E_{\text{sol}})$ is the solution energy, and $n^{\alpha}(\epsilon)$ is the solution-energy DOS for the phase α normalized according to Eq. (3). Employing the thus obtained μ , the ratio of interstitial atoms to available interstitial sites in the whole multiphase state, x , is obtained based on Eq. (9). The ratio of interstitial atoms to available interstitial sites in the phase α , x^{α} , is given as

$$x^{\alpha} = \int_{-\infty}^{\infty} n^{\alpha}(\epsilon) f(\epsilon; T, \mu) d\epsilon, \quad (15)$$

and satisfies

$$\sum_{\alpha} y^{\alpha} x^{\alpha} = x. \quad (16)$$

Particularly when considering the coexistence of the fcc and the hcp phases in the limit of $y^{\text{hcp}} \rightarrow 0$, the concentration of interstitial atoms in the vicinity of a stacking fault, x^{SF} , can be approximated by x^{hcp} . This is because interstitial sites at the fcc stacking faults have locally similar configurations of atoms as those in the hcp phase.

E. Local environments around interstitial atoms

Defining a local environment of an interstitial site by the number of atoms each element has in the 1NN shell, there are 210 and 70 inequivalent 1NN configurations for octahedral and tetrahedral sites in CrMnFeCoNi, respectively. For octahedral sites, considering also the inequivalence under rotation and inversion of octahedra, the number of distinct configurations further increases to 680. To investigate the local-environment dependence in detail, we computed the solution energies of in total 1080 octahedral and 324 tetrahedral sites both for the fcc and for the hcp phases. In terms of the local concentrations of the elements in the 1NN shell, 97 and 91% of distinct local chemical environments were covered for the octahedral sites of the fcc and for the hcp phases, respectively, and 97% were covered for the tetrahedral sites of both the two phases. The remaining local environments

are rarely found in the ideal mixing state; for example, in the ideal mixing state of CrMnFeCoNi, an octahedral site with Cr fully occupying the 1NN shell has a very low probability of 0.0064%. Note that a previous computational study for fcc Fe-Mn [54] found that, although the concentration of Mn in the 1NN shell dominates the solution energies of C atoms, the inequivalence of the local environments under rotation and inversion can further affect the solution energies even with the same local Mn concentration.

To analyze the relation between ΔE_{sol} and the 1NN local environment around an interstitial C atom, the following two approaches were applied.

First, we employed linear regressions of ΔE_{sol} based on the atomistic properties around interstitial sites selected as follows. In a previous computational study for fcc Fe-Mn [54], solution energies of C atoms in octahedral sites are found to decrease when the number of Mn atoms in the 1NN shell increases, where Mn has a smaller valence-electron number than Fe. Expecting a similar relation for CrMnFeCoNi, we considered local valence-electron concentration (VEC). The local VEC was computed as the average of valence electron numbers over the six and the four atoms in the 1NN shell of an interstitial atom for octahedral and tetrahedral sites, respectively. The valence electron numbers of Cr, Mn, Fe, Co, and Ni were set as 6, 7, 8, 9, and 10, respectively. Interstitial atoms also cause a compressive stress field inside alloys. To see its impact, the volume of the interstitial atom, V_{int} , is also considered. The V_{int} were computed based on Voronoi tessellation [95]. Atomic charges and atomic magnetic moments were also computed, where we considered the value on each interstitial atom and the average over the atoms in the 1NN shell. The charge and the magnetic moment on each atom are evaluated from the site-projected wave function within radii of 1.3 and 0.9 Å for $3d$ transition elements and C, respectively.

Second, to describe the local chemical environment beyond a local VEC, we applied a local cluster expansion (CE) method [96–99]. In this expansion, the solution energy is expressed as a linear combination of cluster functions, like a typical CE. In contrast to a full CE, only clusters around the interstitial atom are considered. Effective cluster interactions (ECIs) were determined by the least-squares method. Figure 2 shows the clusters around octahedral sites considered in the present local CE. We limited the considered clusters up to three-body interactions, because the number of ECIs dramatically increases for many-body clusters of multicomponent systems. This can cause overfitting or can even result in an underdetermined set of equations. The local CE was performed using an in-house developed code.

F. Electronic-structure calculations

The plane-wave basis projector augmented wave method [100] was employed in the framework of density functional theory (DFT) within the GGA of the Perdew-Burke-Ernzerhof form [101] as implemented in the VASP code [102–104]. The plane-wave cutoff energy was set to 400 eV. The Brillouin zones were sampled by a Γ -centered $4 \times 4 \times 4k$ -point mesh for the 54-atom supercell models, and the Methfessel-Paxton scheme [105] was employed with the smearing width of 0.1 eV. The $3d4s$ orbitals of Cr, Mn, Fe, Co, and Ni and the

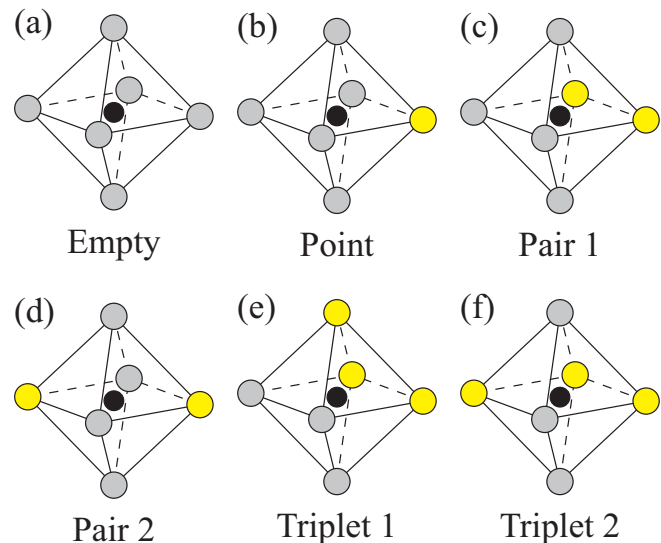


FIG. 2. Clusters considered in the local CE for octahedral sites. The black circle at the center represents the interstitial atom. The surrounding yellow and gray circles represent the lattice atoms included in and excluded from the cluster, respectively.

$2s2p$ orbitals of C were treated as the valence states. The total energies were minimized until they converge within 10^{-3} eV per simulation cell for each ionic step.

For supercells without interstitial atoms, internal atomic positions were initially placed on the exact fcc and hcp lattice sites for the fcc and hcp supercell models, respectively. Ionic relaxations were performed until the residual forces became less than 5×10^{-2} eV/Å. The volumes and the shapes of the supercells were kept fixed to the fcc lattice constant of 3.6 Å, which is close to the experimental value [1,106–111]. The ideal c/a ratio of $\sqrt{8/3} \approx 1.633$ was applied for the hcp phase, as in experiments [110,111] hcp CrMnFeCoNi revealed a c/a ratio close to the ideal one at ambient conditions. In principle, interstitial alloying may also induce lattice expansion, which further affects the SFE. A previous computational study for pure Fe and $\text{Cr}_{0.200}\text{Fe}_{0.716}\text{Ni}_{0.084}$ [45], however, showed that the local impact of C atoms on the SFE is substantially larger than the indirect global impact of lattice expansion (see Figs. 4 and 5 in Ref. [45]). In the present paper, therefore, the impact of the C-induced lattice expansion on the SFE was assumed to be small, and we used the experimental lattice constant throughout the calculations with C-containing alloys.

All calculations have been performed considering spin polarization. Note that, in previous studies, spin-polarized states were found lower in energy as compared to a nonmagnetic (NM) state for equiatomic CrMnFeCoNi both in the fcc and in the hcp phases [78,81,112]. A previous computational study based on the coherent-potential approximation also found that, near the experimental lattice constants, magnetic moments on Cr and Mn are ordered antiparallel to those of Fe, Co, and Ni both for the fcc and for the hcp phases [112]. In the present paper, therefore, all the magnetic moments on Cr and Mn were initially set to be antiparallel to those on Fe, Co, and Ni. As discussed in detail in Sec. III A, the optimized

TABLE I. Computed energies of CrMnFeCoNi (meV/atom) without C atoms in the fcc and in the hcp phases. The reference is set to the energy of the fcc phase at the atomic positions fixed to the ideal fcc lattice sites (shown in parentheses). The columns “Diff.” and “SFE” shows the the energy differences from the fcc to the hcp phases and the corresponding SFEs (mJ/m^2), respectively. The rows “Fixed” and “Relaxed” show the energies at the atomic positions fixed to the ideal lattice sites and at the relaxed atomic positions, respectively. Note that the volumes were fixed to the value corresponding to the fcc lattice constant of 3.6 \AA , as detailed in Sec. II F.

	fcc	hcp	Diff.	SFE
Fixed	(0.0)	2.1	2.1	12
Relaxed	-17.2	-17.9	-0.7	-4

magnetic orientation on each atom is substantially affected by its local environment. Note that previous experimental [113] as well as computational [112,114] studies indicate that CrMnFeCoNi has a very low magnetic transition temperature and is at room temperature in a paramagnetic (PM) state. It is in principle possible to approximate also the PM state using the disordered-local-moment approach in combination with, e.g., SQSs [41,115–120]. For complex multicomponent alloys like CrMnFeCoNi studied here, however, such calculations are computationally rather challenging and require highly demanding approaches such as constrained spin DFT. In the present paper, since we are mainly interested in chemical trends, we focus on the above-mentioned magnetically ordered state, where Cr and Mn are initialized antiferromagnetically with respect to Fe, Co, and Ni.

For each considered interstitial site, a C atom was first placed at the geometric center, and then the internal atomic positions are reoptimized. To verify that the interstitial atoms have not diffused to another interstitial site after the ionic relaxation, we utilized Steinhardt bond-orientational order parameters [121], as detailed in Appendix A. The impact of zero-point vibrational contributions of C is discussed in Appendix B, while this is not considered in the results of the main part.

III. RESULTS AND DISCUSSION

A. Phase stability and SFE of the interstitial-free CrMnFeCoNi

Before discussing how interstitial C atoms impact alloy properties, we first summarize our computational results for interstitial-free CrMnFeCoNi. The energies of the fcc and the hcp phases were evaluated by taking the average over 120 configurations obtained from element permutations for the given SQS. Table I shows the computed energies of CrMnFeCoNi in the fcc and in the hcp phases. On average, relaxation of internal atomic positions decreases the energies of the fcc and the hcp phases by 17.2 and 20.0 meV/atom, respectively. Such relaxation energies are comparable to other $3d$ -transition-element-based fcc HEAs [122] as well as the body-centered cubic NbMoTaW HEA [123]. Under the AIM1 in Eq. (1), the energy difference between the two phases corresponds to a SFE of $12 \text{ mJ}/\text{m}^2$ before the relaxation of internal atomic positions. Including the relaxation energy, the corresponding SFE becomes slightly negative ($-4 \text{ mJ}/\text{m}^2$).

Previous studies [124–126] also demonstrated a substantial contribution of local lattice distortions in CrMnFeCoNi, and actually local lattice distortions are found to enhance solid solution strengthening [19,125,126]. The present paper reveals that the local lattice distortions may also affect the SFEs and thus ductility.

The negative SFE for CrMnFeCoNi implies that at 0 K the hcp phase is energetically more stable as compared to the fcc phase. This is consistent with a recent experimental study [111] where the hcp phase can be found even above 600 K and transformed into the fcc phase at higher temperatures. In recent experiments [17,69], the SFE of CrMnFeCoNi at room temperature was derived to be in the order of 25–30 mJ/m^2 . The difference between the presently computed SFE at 0 K and the experimental values at room temperature may be partly explained by finite-temperature excitations [12]. In first-principles simulations for 0 K, negative SFEs are rather common for $3d$ -transition-element-based HEAs [76–78,80–82,84,127,128]. Various factors such as lattice vibrations [12,78,81], magnetic fluctuations [12,73,127], chemical short-range order [82], and chemical fluctuations close to the stacking faults [83,128] are known to substantially modify the absolute value of the SFEs. In addition, a recent first-principles study found that a potential Cr sublattice ordering could further increase the SFE of CrCoNi [82]. To focus on the chemical trend of adding C, we assume that these effects partially cancel out when considering the energetic difference between the fcc and the hcp phases to compute SFEs based on the AIM1 in Sec. II A.

B. Impact of C on phase stability and SFE

In this subsection, we discuss the impact of interstitial C atoms on the fcc-hcp phase stability and SFE for CrMnFeCoNi. All the C atoms initially placed on tetrahedral sites were actually found to relax into neighboring octahedral sites or, for the hcp phase, occasionally into neighboring hexahedral sites [129] (see Appendix A for details). Thus, our results clearly indicate that tetrahedral sites of CrMnFeCoNi are not only thermodynamically but also dynamically unstable for C atoms. Previous computational studies showed the same site preference for pure fcc Fe [29], fcc Ni [40,47,50,51], and hcp Co [51]. For fcc Fe [29] and fcc Ni [47,50], furthermore, tetrahedral sites are found to have much lower migration barriers for C atoms than octahedral sites, indicating that the tetrahedral sites are dynamically less stable than the octahedral sites for C atoms. In the following, we exclusively focus on the octahedral sites as possible interstitial sites for C atoms.

Figure 3 shows the distribution of the computed solution energies ΔE_{sol} of the interstitial C atoms at the octahedral sites. The standard deviations of the ΔE_{sol} distributions are 0.232 and 0.228 eV for the fcc and the hcp phases, respectively, and the differences between the highest and the lowest ΔE_{sol} are larger than 1.5 eV. These ΔE_{sol} fluctuations are larger than, e.g., the thermal energy at relevant annealing temperatures (approximately 0.1 eV at 1000 K). This indicates that the impact of thermal excitations of C atoms from low- to high-energy configurations is rather limited and thus that this local-environment dependence of ΔE_{sol} can substantially impact on thermodynamic properties.

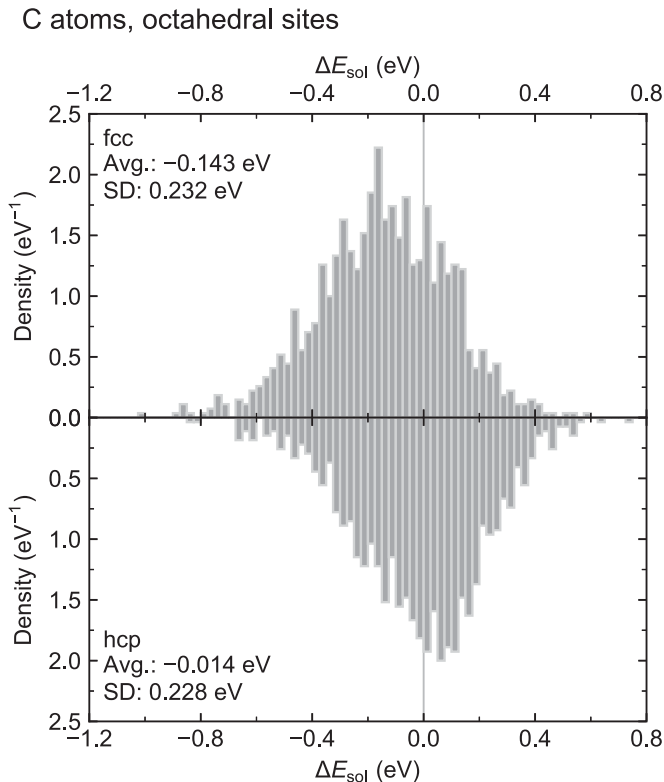


FIG. 3. Distribution of computed solution energies ΔE_{sol} of interstitial C atoms at the octahedral sites in CrMnFeCoNi. The upper and the lower panels show the results for the fcc and the hcp phases, respectively. The average (avg.) and the standard deviation (SD) of ΔE_{sol} are also shown in the panels.

Employing the formalism in Sec. II C together with the computed solution-energy DOS, energetic stabilities of the fcc and the hcp phases are next compared for the two extreme thermodynamic conditions. In the ideal quenched condition, where the C atoms are equally distributed over all interstitial sites independent of the corresponding solution energies, the impact C atoms have on the SFE [Eq. (4)] is given by the average solution energy $\overline{\Delta E}_{\text{sol}}$ [Eq. (7)]. As shown in Fig. 3, $\overline{\Delta E}_{\text{sol}}$ is by 0.129 eV lower in the fcc phase than in the hcp phase. This implies that, in the ideal quenched condition, C atoms energetically strengthen the fcc phase more than the hcp phase. Based on the AIM1 [Eq. (4)], an energy difference of 0.129 eV corresponds to a SFE change of 35 and 7 mJ/m² for 1 wt. % and for 1 at. % of C atoms, respectively. This value is much lower than the corresponding values for pure fcc Fe, 300–400 mJ/m² for 1 wt. % of C atoms in first-principles simulations [37,39,55,59] and 410 mJ/m² for 1 wt. % of C atoms in experiments [130,131]. In a recent experimental study on CrCoNi [26], the SFE increases by approximately 55 mJ/m² for 1 wt. % C. This value is much closer to our current one obtained for CrMnFeCoNi and also much smaller than the one found for pure fcc Fe.

In order to elucidate why C atoms have a much smaller impact on SFEs for these HEAs than on pure Fe, we performed additional SFE calculations for pure Cr, Mn, Fe, Co, and Ni. The supercell models with the same cell shape as those for CrMnFeCoNi were employed for these calculations. We

compute 17 lattice constants from 3.2 to 4.0 Å and then determine the equilibrium lattice constants by fitting the energy-volume relations to the Vinet equation of state [132,133]. Since we are mainly interested in general trends among elements, we focus only on the NM state for the five elements and on the ferromagnetic (FM) state for Co and Ni.

Table II summarizes the thus obtained impact C atoms have on the SFEs of pure Cr, Mn, Fe, Co, and Ni. We first confirm that the equilibrium lattice constants are close to those obtained previously [39,55,134–136], that C solution energies in the fcc phase are also consistent with those in previous reports [47,50], and that the impact of C atoms on the SFE of pure Fe in the present paper is close to those reported in the previous computational studies [37,39,55,59]. From the comparison among the considered five 3d elements, it is found that Fe indeed shows the strongest impact of C atoms on the SFE both at the equilibrium fcc lattice constants and at the experimental fcc lattice constant of CrMnFeCoNi (3.6 Å) [1,106–111]. The other elements show much smaller (and sometimes even negative) SFE changes when alloying with C. This qualitatively explains the reduced impact of C atoms on the SFEs of CrMnFeCoNi and CrCoNi simply as the reduction of the Fe concentration in these HEAs. Averaging the C-induced change in the SFE over the five pure elements, we obtain 46 and 10 mJ/m² for 1 wt. % and 1 at. % C, respectively (see Table II). These values are surprisingly close to those obtained explicitly for CrMnFeCoNi in the ideal quenched condition, where various local environments around C are considered. Specifically, the deviation from the average over pure elements is –24%. This suggests that a rough estimate of the C impact on the SFEs of HEAs may be obtained from those of pure metals, which is a computationally much simpler task.

We next consider the ideal annealed condition, where C atoms in each phase are distributed not randomly but according to the solution energy of each interstitial site. In this case, the impact of the interstitial C atoms on the Helmholtz energy, $\Delta F_{\text{sol}}(T, x)$ [Eq. (5)], depends on temperature T and concentration x . Figure 4(a) shows the difference of $\Delta F_{\text{sol}}(T, x)$ per C atom from the fcc to the hcp phases. It is found that $\Delta F_{\text{sol}}(T, x)$ is lower in the fcc phase than in the hcp phase in the wide region of temperature and C concentration, indicating that interstitial C atoms thermodynamically stabilize the fcc phase of CrMnFeCoNi also in this thermodynamic condition. In the AIM1 [Eq. (4)], this again corresponds to the increase of the SFE for the considered ideal annealed condition, if the C concentration remains the same in the vicinity of stacking faults and in the bulk region. For increasing T and for increasing x , the difference of ΔF_{sol} between the fcc and the hcp phases approaches the value in the ideal quenched condition, 0.129 eV, as expected analytically (Sec. II C). In contrast to the variations in the solution energies, variations of $\Delta F_{\text{sol}}^{\text{hcp}} - \Delta F_{\text{sol}}^{\text{fcc}}$ are much smaller (only 20 meV) at lower temperatures and at lower concentrations. This is probably because the solution-energy DOSs of the two phases largely overlap. Figure 4(b) shows the SFE changes in the ideal annealed condition at given T and x . The SFEs are found to be almost independent of temperature T and to increase almost linearly with respect to the concentration x . For the same x , the SFE shifts due to C are almost identical between the ideal

TABLE II. Impact of C atoms for pure Cr, Mn, Fe, Co, and Ni in the fcc and the hcp phases obtained from first-principles calculations. The column “ a^{fcc} ” shows the fcc lattice constants when the solution energies of C atoms and their impact on the SFEs were evaluated. In addition to the fcc equilibrium lattice constants (asterisk), also the experimental fcc lattice constant of CrMnFeCoNi, 3.6 Å (dagger) [1,106–111], is considered. The columns “ ΔE_{sol} ” show the solution energies of a C atom at the octahedral sites. The columns “ ΔSFE ” show the SFE change due to C. The row “Average” shows the average values over NM Cr, NM Mn, NM Fe, FM Co, and FM Ni. The row “CrMnFeCoNi” shows the values explicitly obtained for CrMnFeCoNi in the ideal quenched condition.

	Magnetic state	a^{fcc} (Å)	ΔE_{sol} (eV)			ΔSFE (mJ/m ²)	
			fcc	hcp	Difference	1 wt. %	1 at. %
Cr	NM	3.608*	−0.798	−1.112	−0.313	−78	−18
		3.600†	−0.713	−1.048	−0.334	−83	−19
Mn	NM	3.496*	−0.231	−0.058	0.173	48	11
		3.600†	−1.193	−1.025	0.169	44	10
Fe	NM	3.447*	0.150	1.253	1.103	323	69
		3.600†	−1.228	−0.266	0.962	258	55
Co	NM	3.451*	0.517	0.954	0.436	134	27
		3.600†	−0.779	−0.404	0.375	106	22
	FM	3.520*	0.491	0.665	0.173	51	10
	3.600†	0.061	0.169	0.108	31	6	
Ni	NM	3.511*	0.188	0.105	−0.083	−25	−5
		3.600†	−0.453	−0.523	−0.070	−20	−4
	FM	3.519*	0.702	0.655	−0.047	−14	−3
Average		3.600†	−0.584	−0.414	0.170	46	10
CrMnFeCoNi		3.600†	−0.143	−0.014	0.129	35	7

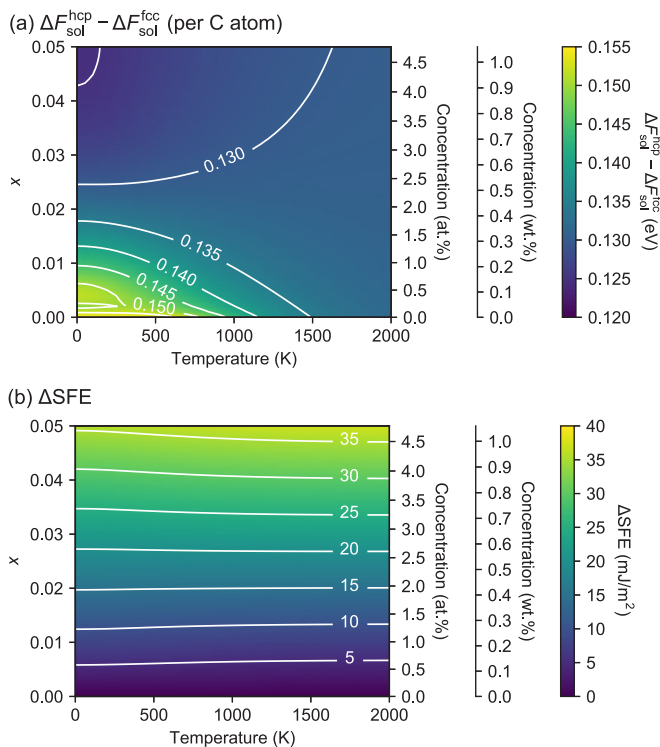


FIG. 4. Impact of C atoms on the solution-energy difference and on the SFE in CrMnFeCoNi as a function of temperature T and concentration x in the ideal annealed condition. (a) Difference of the Helmholtz-energy change $\Delta F_{\text{sol}}(T, x)$ due to one C atom between the fcc and the hcp phases. (b) SFE change due to x concentration of C at given T .

quenched and the ideal annealed conditions. This is, again, a consequence of the large overlap of solution-energy DOSs for the fcc and the hcp phases.

We therefore conclude that in both the thermodynamic limits C is found to increase the SFE of fcc CrMnFeCoNi. This finding is supported by recent experimental studies that reported a C-induced increase of the SFE for CrMnFeCoNi [18], Cr_{0.1}Mn_{0.3}Fe_{0.5}Co_{0.1} [10], and CrCoNi [26].

The C-induced increase of SFEs shown above implies that placing C at the stacking faults of CrMnFeCoNi is thermodynamically unfavorable. Thus, there exists a thermodynamic driving force for C atoms to segregate away from the stacking faults towards the fcc bulk region. This can be regarded as an anti-Suzuki behavior. To quantitatively evaluate this effect, the local C ratio in the vicinity of stacking faults, x^{SF} , is estimated giving the same chemical potential of C both for the bulk region and for the stacking faults as described in Sec. IID. Figure 5 shows the thus obtained x^{SF} and its ratio to the bulk concentration x . The ratio x^{SF}/x is always smaller than 1, revealing an antisegregation behavior, i.e., a segregation tendency of C away from the stacking faults. For instance, x^{SF} is less than 20% of x around room temperature and around 0.1 wt. % of C concentration. As shown in Fig. 4(b), the depletion of C concentration near the stacking faults reduces the SFE. This SFE reduction thermodynamically stabilizes the stacking faults.

C. Local environment around C

We next analyze the dependence of ΔE_{sol} on the local environment around the interstitial C atom in more detail. For the first qualitative measure, we focus on “ M -rich environments” ($M = \text{Cr, Mn, Fe, Co, Ni}$) where the element

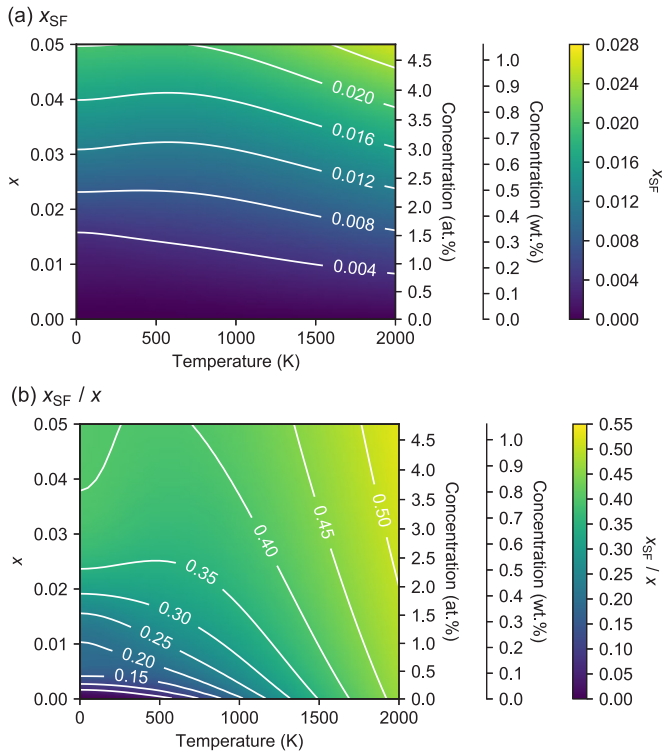


FIG. 5. Ratio of the number of C atoms to the number of available interstitial sites at the stacking faults, x^{SF} , as a function of temperature, T , and C ratio in the bulk region, x , when considering the same chemical potential of C both for the bulk region and for the stacking faults according to Sec. IID. (a) Raw x^{SF} . (b) Ratio of x^{SF} to x .

M occupies half or more of the 1NN atomic sites around a C atom. Figure 6 shows the distributions of ΔE_{sol} for the M -rich local chemical environments. The distribution of ΔE_{sol} depends sensitively on the various local chemical environments. Cr-rich environments tend to show lower solution energies, followed by Mn-rich, Fe-rich, Co-rich, and Ni-rich environments. Particularly in Ni-rich environments, solution energies tend to be positive, indicating that the dissolution of C atoms from the considered reference graphite state into Ni-rich octahedral sites in CrMnFeCoNi is endothermic. This finding links to previous computational studies [47,50] that revealed an endothermic dissolution of C atoms for pure fcc Ni. The low solution energies in Cr-rich environments indicate that, if C atoms in CrMnFeCoNi diffuse sufficiently, they are more likely in Cr-rich interstitial sites than in other local environments. Indeed, previous experimental studies [10,18] reported Cr-rich $M_{23}C_6$ ($M = \text{Cr, Mn, Fe, Co, Ni}$) carbides for $\text{Cr}_{0.1}\text{Mn}_{0.3}\text{Fe}_{0.5}\text{Co}_{0.1}$ and CrMnFeCoNi when alloyed with additional interstitial C. Our results suggest that the creation of Cr-rich carbides in these HEAs is promoted by C atoms preferentially going into the energetically favorable Cr-rich environments.

In order to further understand and quantify the chemical trends of solution energies ΔE_{sol} , their correlations with the atomistic properties introduced in Sec. IIE are next analyzed. Table III shows the root-mean-square errors (RMSEs) and the correlation coefficients r between the C solution

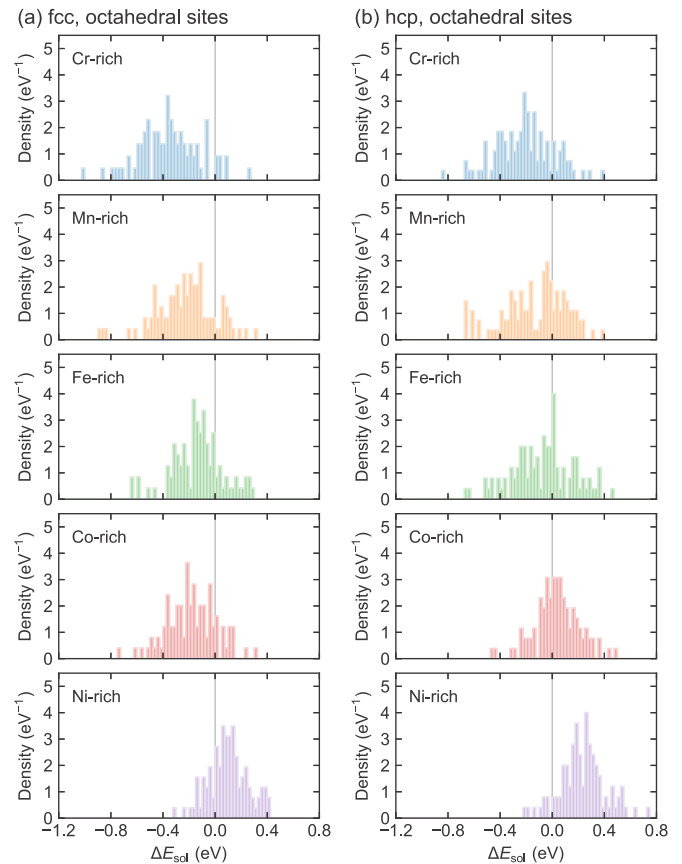


FIG. 6. Distributions of the computed solution energies ΔE_{sol} of C atoms at octahedral sites in M -rich 1NN local chemical environments ($M = \text{Cr, Mn, Fe, Co, Ni}$) for the (a) fcc and the (b) hcp phases of CrMnFeCoNi.

energies ΔE_{sol} obtained from our first-principles calculations and those predicted by linear regressions based on the atomistic properties. The local VEC in the 1NN shell of the C atom, $\text{VEC}_{1\text{NN}}$, shows the strongest correlation with ΔE_{sol} among the considered properties, as quantified by the correlation coefficients of 0.511 and 0.597 for the fcc and the hcp phases,

TABLE III. Relations between ΔE_{sol} obtained by first-principles calculations and those predicted by the linear regressions based on atomistic properties for C atoms at octahedral sites. The columns r show the correlation coefficients. $\text{VEC}_{1\text{NN}}$: local VEC in the 1NN shell of the C atom. V_{int} : Voronoi volume of the interstitial atom [95]. ρ_{int} : charge of the interstitial atom. $\rho_{1\text{NN}}$: average charge of the atoms in the 1NN shell. m_{int} : magnetic moment of the interstitial atom. $m_{1\text{NN}}$: average magnetic moments of the atoms in the 1NN shell.

	RMSE (eV)		r	
	fcc	hcp	fcc	hcp
$\text{VEC}_{1\text{NN}}$	0.199	0.183	0.511	0.597
V_{int}	0.206	0.196	0.458	0.505
ρ_{int}	0.214	0.199	0.385	0.489
$\rho_{1\text{NN}}$	0.231	0.228	0.081	0.014
m_{int}	0.227	0.226	0.201	0.135
$m_{1\text{NN}}$	0.227	0.225	0.192	0.149

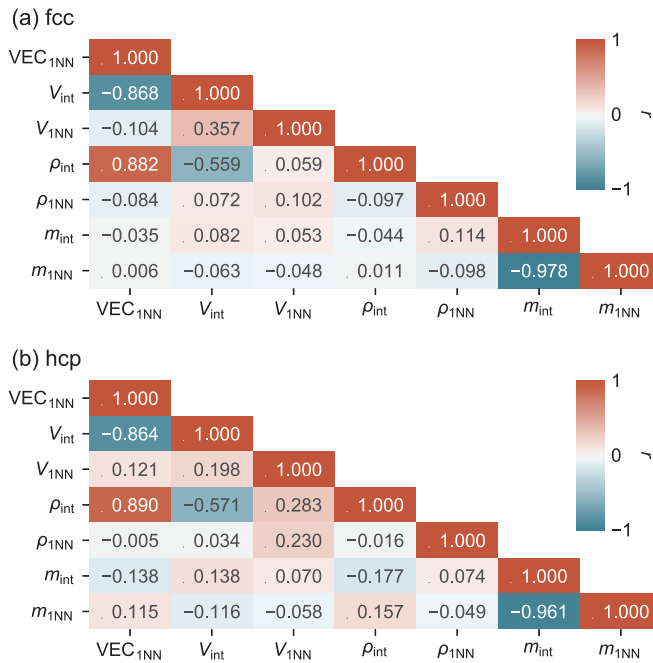


FIG. 7. Correlation matrices for the atomistic properties around the interstitial C atoms for the (a) fcc and the (b) hcp phases.

respectively. A similar trend was also found for fcc Fe-Mn in a previous computational study [54], where solution energies of C atoms in octahedral sites decrease when the number of Mn atoms in the 1NN shell increases. Substantial correlations with ΔE_{sol} are found also for the Voronoi volume V_{int} of the interstitial C atom. This implies that elastic interactions between C and host lattice atoms contribute to ΔE_{sol} . The charge of the C atom, ρ_{int} , also shows a substantial correlation with ΔE_{sol} . This indicates that the charge transfer between C atoms and host lattice atoms also contributes to ΔE_{sol} . In contrast, almost no correlations with ΔE_{sol} are found for the magnetic moment of the C atom and that in the 1NN shell of the C atom.

Interestingly, the $\text{VEC}_{1\text{NN}}$, a simple value that can be obtained without first-principles calculations, shows the strongest correlation with the C solution energy among all the investigated local atomistic properties. To elucidate the relation between $\text{VEC}_{1\text{NN}}$ and the other considered atomic properties, correlation coefficients r among them are computed and shown in Fig. 7. It is found that $|r|$ is close to 1 between $\text{VEC}_{1\text{NN}}$ and V_{int} and between $\text{VEC}_{1\text{NN}}$ and ρ_{int} , meaning that $\text{VEC}_{1\text{NN}}$ strongly correlates with both V_{int} and ρ_{int} . This shows that these two properties depend on the $\text{VEC}_{1\text{NN}}$ almost linearly. It is therefore expected that both the elastic interaction and charge transfer between C and host lattice atoms can be in practice very efficiently derived by considering $\text{VEC}_{1\text{NN}}$.

The observed correlations between solution energies and local VEC indicate that the variation of C solution energies in CrMnFeCoNi is mainly caused by local chemical effects. To further analyze this, we evaluated the local chemical environment by applying a local CE method. Table IV shows the RMSEs and the correlation coefficients r between ΔE_{sol} obtained from the first-principles calculations and those predicted by

TABLE IV. Relations between ΔE_{sol} obtained by first-principles calculations and those predicted by the local CE method for C atoms at octahedral sites. The first column shows the labels of the local clusters in Fig. 2 considered in the local CE method, and the second column shows the number of ECIs for the local clusters. The columns r show the correlation coefficients.

	No. of ECIs	RMSE (eV)		r	
		fcc	hcp	fcc	hcp
(a), (b)	5	0.192	0.177	0.558	0.629
(a)–(c)	21	0.186	0.172	0.597	0.654
(a)–(d)	37	0.184	0.170	0.606	0.663
(a)–(c), (e)	85	0.184	0.171	0.611	0.660
(a)–(f)	165	0.178	0.165	0.638	0.690

the local CE method. As the number of the descriptors for the local chemical environment increases, the correlations of the predicted solution energies ΔE_{sol} with those obtained from first-principles calculations are enhanced. The enhancements from the local-VEC prediction are, however, not very large; the improvement of the RMSE is only about 0.02 eV both for the fcc and for the hcp phases, even when considering all the 1NN clusters in Fig. 2. This indicates that the local VEC is already an excellent descriptor capturing most of the interactions. Even when all the 1NN clusters in Fig. 2 are considered, the correlation coefficients are still below 0.7. This indicates that interactions beyond the 1NN shell are substantial and contribute about one-third. To obtain a further better parametrization of local chemical environments, interactions beyond the 1NN shell must be considered.

Finding the large dependence on the local chemical environment, we finally focus on the difference of ΔE_{sol} between the fcc and the hcp phases for individual local chemical environments. Here, the 1NN local chemical environment is described by the numbers of chemical elements in the 1NN shell. Note that, for a given local chemical environment, the solution energy shows a large standard deviation. This nonuniqueness of the solution energy on the specific 1NN environment should be caused by long-ranged chemical or magnetic interactions beyond the 1NN shell. We therefore focus on the average solution energy for each local chemical environment. Figure 8 shows the results. For most of the 1NN local chemical environments, the average ΔE_{sol} are found higher in the hcp phase than in the fcc phase. This indicates that most of the local chemical environments contribute to the increase of SFE for CrMnFeCoNi when C atoms are added. Assuming the same trend, the increase of SFE by the addition of C atoms is expected also for alloys with modified compositions, because such alloys offer similar local chemical environments. Figure 8 also again confirms that local chemical environments with higher VEC tend to have higher ΔE_{sol} .

IV. CONCLUSIONS

We studied interstitial C solution in the prototypical CrMnFeCoNi HEA by employing first-principles calculations scanning over various chemically different local environments. We considered 1080 and 324 different C configurations for

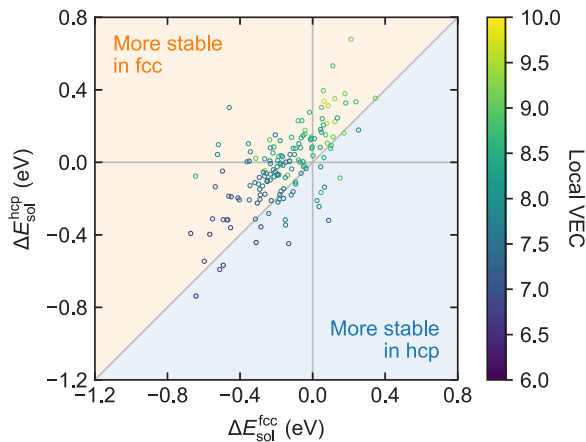


FIG. 8. Comparison of ΔE_{sol} between the fcc and the hcp phases for each 1NN local chemical environment. The symbols are colored according to the local VEC of the corresponding local environments.

the two fundamental interstitial configurations, octahedral and tetrahedral, respectively, for both the fcc and hcp phases. Based on this vast amount of first-principles data, a highly realistic representation of the stability and the energetics of interstitial C in CrMnFeCoNi could be obtained.

(1) C atoms initially placed at tetrahedral sites go into octahedral sites after relaxation, implying that C at tetrahedral sites in CrMnFeCoNi is dynamically unstable.

(2) The distribution of the interstitial C solution energies shows a width of more than 1.5 eV, which is an order of magnitude larger than the thermal energy at relevant annealing temperatures (approximately 0.1 eV at 1000 K). This indicates that the impact of thermal excitations of C atoms from low- to high-energy configurations is rather limited. The large variation of solution energies also indicates the strong dependence of them on the local environment of C.

(3) The obtained C solution-energy DOS allows us to consider two thermodynamic limits for the C impact on the phase stability and the stacking-fault energy; one assumes a fully random occupation of C atoms irrespective of the solution energies in different local environments (the ideal quenched condition), and the other assumes that C atoms are distributed according to a canonical ensemble for the solution energies (the ideal annealed condition).

(4) In both the considered thermodynamic limits, C in CrMnFeCoNi is found to increase the SFE, which is consistent with the trends in experiments for 3d-transition-element HEAs [10,18,26]. In the ideal quenched condition, the SFE change is 35 and 7 mJ/m² for 1 wt. % and for 1 at. % of C, respectively. In the ideal annealed condition, the SFE change is almost the same as those in the ideal quenched condition at the same C concentrations and is almost independent of temperature.

(5) From the analysis of the correlations between C solution energies and the local environment, C in CrMnFeCoNi is found to energetically prefer the interstitial sites with lower local valence-electron concentration. This particularly suggests that the creation of Cr-rich carbides in 3d-transition-element HEAs [10,18] is promoted by C atoms preferentially segregating into the energetically favorable Cr-rich environments.

The strong dependence of the C impact on the local chemical environment indicates that interstitial alloying with controlling the total or even local chemical composition (e.g., introducing a certain degree of chemical short-range order) is a promising strategy to tune the SFE of HEAs. We also emphasize that such a strong dependence of C solution energies on local environments may be found not only for HEAs but also for other alloys like, e.g., Fe-Mn steels. In contrast to pure metals, therefore, it is decisive to exhaustively screen the phase space spanned by the different local chemical environments to derive conclusions regarding the phase stability for such alloys.

ACKNOWLEDGMENTS

We thank Andrei V. Ruban for sharing his code to generate the SQSs, Liam Huber for sharing his code to compute Steinhardt bond-orientational order parameters, as well as Tilmann Hickel, Zhiming Li, Xiaoxiang Wu, and Dierk Raabe for fruitful discussion. Funding from the Deutsche Forschungsgemeinschaft (Grant No. SPP 2006); from the Ministry of Education, Culture, Sports, Science, and Technology, Japan, through the Elements Strategy Initiative for Structural Materials of Kyoto University; and from a Grant-in-Aid for Scientific Research on Innovative Areas, “Nano Informatics” (Grant No. 25106005), from the Japan Society for the Promotion of Science is gratefully acknowledged.

APPENDIX A: IDENTIFICATION OF THE GEOMETRY OF INTERSTITIAL SITES

Unlike pure metals or ordered alloys, it is not straightforward to identify the geometry around interstitial atoms for supercell models of disordered alloys with relaxed atomic positions, because in general the lattice atoms are actually not at the ideal lattice sites. This issue is particularly critical if the interstitial atom is dynamically unstable at the initially expected interstitial site, because then, after the relaxation of atomic positions, the interstitial atom actually sits on a neighboring dynamically stable interstitial site. Although it is possible to identify the geometry of interstitial sites by visualizing atomic positions, such a strategy requires an impractical amount of human cost when thousands of interstitial sites must be inspected.

To overcome this difficulty, we utilized Steinhardt bond-orientational order parameters [121] for the identification of the geometry of interstitial sites. The l th order of Steinhardt bond-orientational parameters for an atom is computed as

$$Q_l = \sqrt{\frac{4\pi}{2l+1} \sum_{m=-l}^{+l} |q_{lm}|^2}, \quad (\text{A1})$$

$$q_{lm} = \frac{1}{N} \sum_{i=1}^N Y_l^m(\mathbf{r}_i), \quad (\text{A2})$$

where N is the number of considered neighboring atoms, \mathbf{r}_i is the vector pointing to the i th atoms in the neighbors, $Y_l^m(\mathbf{r}) = Y_l^m(\theta, \phi)$ are spherical harmonics [137], and θ and ϕ are the angular coordinates corresponding to \mathbf{r} . These parameters are useful descriptors of local environments for

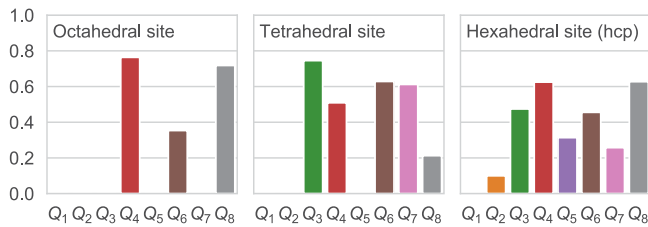


FIG. 9. Steinhardt bond-orientational order parameters from Q_1 to Q_8 for the ideal octahedral (left) and the ideal tetrahedral (center) sites in the fcc and in the hcp phases, as well as for the ideal hexahedral (right) sites in the hcp phase.

substitutional segregation at grain boundaries [138,139]. Here we calculated Steinhardt bond-orientational order parameters using the CLUSTERGB code [138,140,141].

We first computed reference values of Steinhardt bond-orientational order parameters for the ideal interstitial sites where the atoms are fixed to ideal lattice sites. Figure 9 shows the Steinhardt bond-orientational parameters for the ideal octahedral and the ideal tetrahedral sites surrounded by six and four neighboring atoms, respectively. For the hcp phase, we can also consider the hexahedral sites surrounded by five neighboring atoms [129], which has actually a similar local configuration to the $\Sigma[1\bar{1}0](111)$ symmetric tilt grain boundary in the fcc phase. The Steinhardt bond-orientational order parameters for the ideal hexahedral sites in the hcp phase are also shown in Fig. 9. Within $l \leq 8$, Q_3 shows the largest difference between the ideal octahedral and the ideal tetrahedral sites. We therefore focused on Q_3 and computed it for the C atoms after the relaxation of atomic positions. We computed Q_3 with six, four, and five neighboring atoms, which are then compared with Q_3 of the ideal octahedral, ideal tetrahedral, and ideal hexahedral sites, respectively. If, e.g., the difference was the smallest for the comparison with the ideal octahedral sites, the C position was identified as an octahedral site.

All the C atoms initially put on octahedral sites are found to remain on octahedral sites. This indicates that C atoms at octahedral sites are dynamically stable in CrMnFeCoNi. In contrast, all the C atoms initially put on tetrahedral sites diffuse to other kinds of neighboring interstitial sites after the ionic relaxation. This indicates that C atoms at tetrahedral sites are dynamically unstable in CrMnFeCoNi. For the fcc phase, all such C atoms diffused to octahedral sites. For the hcp phase, among 324 C atoms, 248 (77%) diffused to octahedral sites, and the remaining 76 (23%) were found at hexahedral sites in the hcp phase after the ionic relaxation.

A hexahedral site in the hcp phase has a similar local configuration of atoms to the $\Sigma 3[1\bar{1}0](111)$ symmetric tilt grain boundary of the fcc phase. The result above therefore implies that C atoms are dynamically stable also at the $\Sigma 3[1\bar{1}0](111)$ symmetric tilt grain boundary in fcc CrMnFeCoNi. To analyze the energetic stability of the C atoms at hexahedral sites, we also computed the solution energies ΔE_{sol} of the 76 C atoms at the hexahedral sites, as shown in Fig. 10. Compared with the results for octahedral sites in Fig. 3, the ΔE_{sol} at hexahedral sites are clearly prone to be higher than those at octahedral sites. This indicates that, although the C atoms are

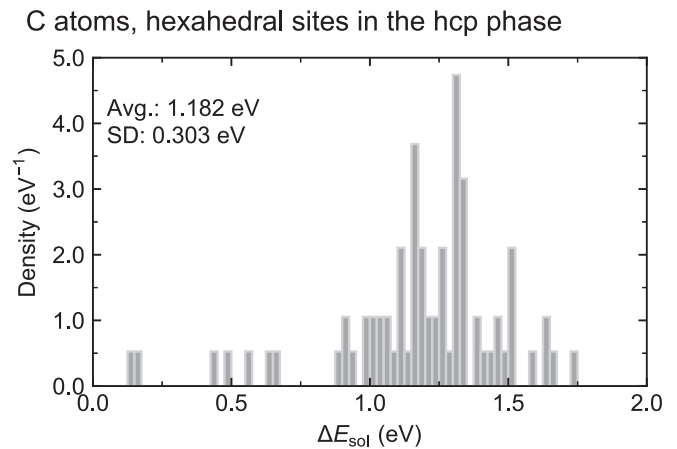


FIG. 10. Distribution of computed solution energies ΔE_{sol} of interstitial C atoms at the hexahedral sites in hcp CrMnFeCoNi. The average (avg.) and the standard deviation (SD) of ΔE_{sol} are also shown in the panels.

dynamically stable at the hexahedral sites in the hcp phase, the C atoms are energetically less likely to be there and more likely to be at octahedral sites. Therefore, we decided to focus on octahedral sites in the main text.

APPENDIX B: ZERO-POINT VIBRATIONAL ENERGIES OF C

Since C is a relatively light element, it is in principle possible that its energy contribution stemming from zero-point

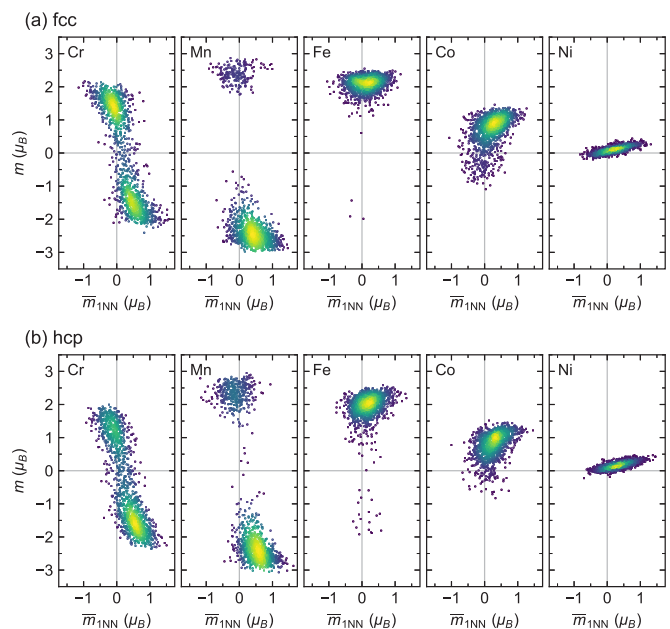


FIG. 11. Distributions of computed atomic magnetic moments in interstitial-free CrMnFeCoNi as a function of the average magnetic moments over the 12 atoms in the 1NN shell for the (a) fcc and the (b) hcp phases. The results for Cr, Mn, Fe, Co, and Ni are shown from left to right. The colors of the symbols denote the densities at the corresponding points determined from Gaussian kernel density estimation, where brighter colors indicate higher densities.

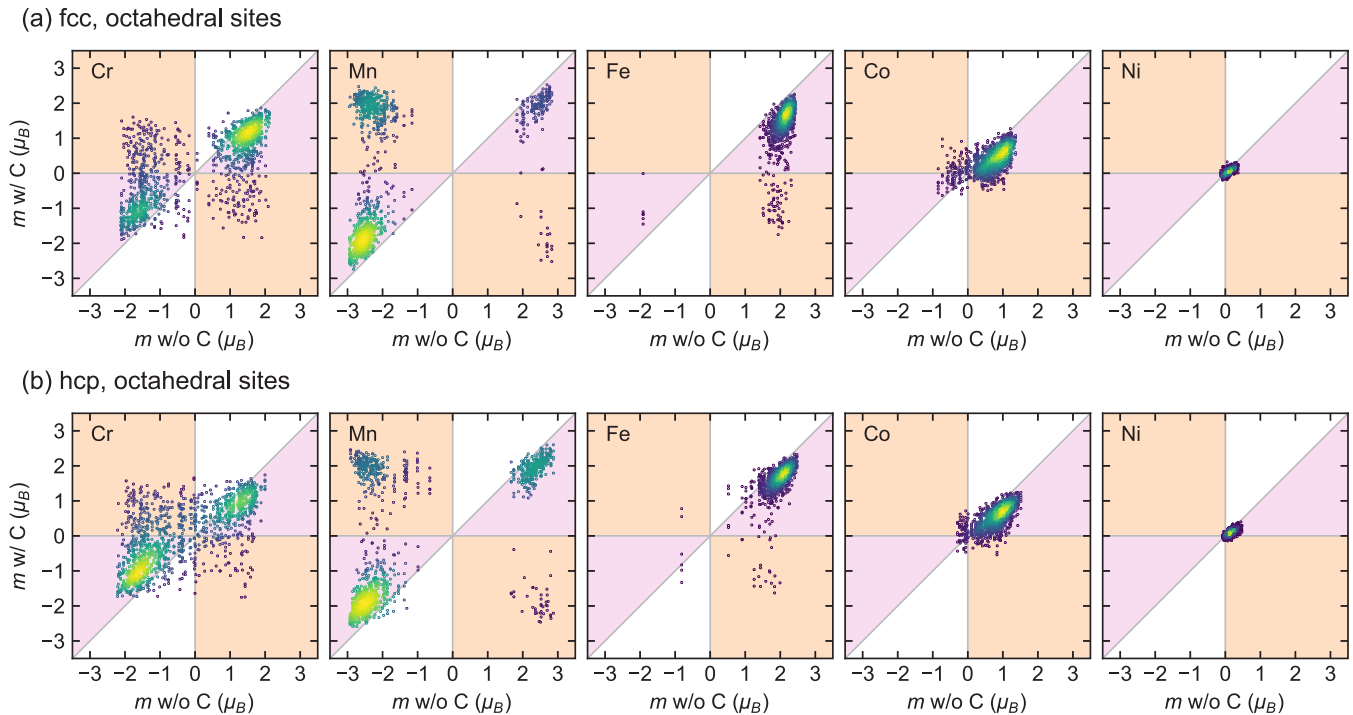


FIG. 12. Impact of C at octahedral sites on the local magnetic moments in the 1NN shell. The x and the y axes show the atomic magnetic moments in the absence and in the presence of C, respectively. (a, b) The fcc and the hcp phases, respectively. The results for Cr, Mn, Fe, Co, and Ni are shown from left to right. The colors of the symbols denote the densities at the corresponding points determined from Gaussian kernel density estimation, where brighter colors indicate higher densities. The pink-shaded regions indicate that the magnetic moments are reduced due to the presence of the interstitial C atoms. The orange-shaded color marks the region where the magnetic moments flip their orientations due to the neighboring C atoms.

vibrations contributes to the solution energy and could impact the SFE. Here we therefore investigate the C contribution to the zero-point vibrational energies (ZPVEs). In principle, ZPVEs can be computed by obtaining phonon frequencies from full harmonic force constants. For supercell models of disordered alloys, however, this is computationally demanding due to their low structural symmetries. To reduce the computational cost, the contributions of ZPVEs on the C solution energies are estimated under the assumptions that the contributions of an interstitial C atom and the matrix to the lattice vibrations can be separated due to the large mass difference and that the matrix contribution is the same between the models with and without the C atom. The contribution of C in CrMnFeCoNi to the ZPVE is then computed based on the model where the C atom vibrates in the matrix fixed to its relaxed internal atomic position. For each C atom in an octahedral site, a 3×3 harmonic force-constant matrix was computed by applying six different displacements of C of 0.01 \AA and then by employing the least-squares method to fit the harmonic force-constant matrix. From the thus obtained force constants, three C frequencies were obtained, and then the C contribution to the ZPVE was computed from these frequencies. This approach was applied to 54 octahedral sites both for the fcc and for the hcp phases. For diamond, the reference state of C, full harmonic force constants were computed by applying the finite displacement of 0.01 \AA to the $3 \times 3 \times 3$ supercell of the eight-atom cubic conventional unit cell. The PHONOPY code [142] was employed for this calculation.

The C contributions to the ZPVEs averaged over the 54 octahedral sites are 0.111 and 0.114 eV/atom for the fcc and the hcp phases, respectively. The difference is 0.003 eV/atom , which is just 2% of the solution-energy difference between the fcc and the hcp phases without the ZPVEs, 0.129 eV/atom (Fig. 3). This indicates that, according to the AIM1 in Eq. (4), the contribution of the ZPVEs to the SFE is negligible. The standard deviations of the C contributions to the ZPVEs are 0.003 eV/atom both for the fcc and for the hcp phases, which is just 1% of the standard deviations of the C solution energies without the ZPVEs, 0.232 and 0.228 eV/atom for the fcc and the hcp phases, respectively (Fig. 3). This indicates that the C contributions to the ZPVEs are almost independent of the local environments of C. The ZPVE of diamond was obtained as 0.181 eV/atom , which is consistent with a previous first-principles study [38]. According to Eq. (2), the C solution energies are estimated to be lower by 0.070 and 0.067 eV/atom for the fcc and for the hcp phases, respectively, when the ZPVEs are considered.

APPENDIX C: MAGNETIC MOMENTS IN CrMnFeCoNi

A previous computational study [81] found that the SFE of CrMnFeCoNi is strongly affected by its magnetic state. It could therefore be of interest to see the magnetic moments in CrMnFeCoNi and the impact of C on them, which are summarized here.

Figure 11 shows distributions of computed atomic magnetic moments in the interstitial-free CrMnFeCoNi as a function of the average magnetic moments over the 12 atoms in the 1NN shell. The results are obtained from the 6480 atoms in the 120 SQS-based configurations both for the fcc and for the hcp phases. The magnetic moments of Cr and Mn are distributed more widely than those of Fe, Co, and Ni, consistent with previous computational studies for CrMnFeCoNi-based equiatomic alloys [81,143–145]. Particularly, the orientations of the magnetic moments of Cr and Mn tend to be opposite to those of the average magnetic moments over their 1NN atoms. This indicates that the magnetic moments of Cr and Mn prefer to be ordered *locally* antiferromagnetically with

respect to the magnetic moments of the 1NN atoms. A similar behavior was found for the magnetic moments of Cr in fcc equiatomic CrFeCoNi [143].

Figure 12 shows the magnetic moments in the 1NN shell of the interstitial C atoms at octahedral sites as a function of the magnetic moments of the same atoms but without C atoms. For Cr and Mn, more than 20% of the atoms flip their spin orientation in the presence of C (found in the orange-shaded region in Fig. 12). It is also found that C atoms often reduce the local magnetic moments in the surrounding 1NN shell (found in the pink-shaded region in Fig. 12). Previous studies for fcc Fe [34,41,42,45] and fcc Ni [47,50] reported a similar depletion of the magnetic moments in the 1NN shell due to C atoms.

-
- [1] B. Cantor, I. Chang, P. Knight, and A. Vincent, *Mater. Sci. Eng. A* **375**, 213 (2004).
- [2] A. Gali and E. George, *Intermetallics* **39**, 74 (2013).
- [3] F. Otto, A. Dlouhý, C. Somsen, H. Bei, G. Eggeler, and E. George, *Acta Mater.* **61**, 5743 (2013).
- [4] B. Gludovatz, A. Hohenwarter, D. Catoor, E. H. Chang, E. P. George, and R. O. Ritchie, *Science* **345**, 1153 (2014).
- [5] G. Laplanche, A. Kostka, O. Horst, G. Eggeler, and E. George, *Acta Mater.* **118**, 152 (2016).
- [6] Z. Wu, H. Bei, G. Pharr, and E. George, *Acta Mater.* **81**, 428 (2014).
- [7] B. Gludovatz, A. Hohenwarter, K. V. S. Thurston, H. Bei, Z. Wu, E. P. George, and R. O. Ritchie, *Nat. Commun.* **7**, 10602 (2016).
- [8] G. Laplanche, A. Kostka, C. Reinhart, J. Hunfeld, G. Eggeler, and E. George, *Acta Mater.* **128**, 292 (2017).
- [9] Z. Li, K. G. Pradeep, Y. Deng, D. Raabe, and C. C. Tasan, *Nature (London)* **534**, 227 (2016).
- [10] Z. Li, C. C. Tasan, H. Springer, B. Gault, and D. Raabe, *Sci. Rep.* **7**, 40704 (2017).
- [11] Z. Li, C. C. Tasan, K. G. Pradeep, and D. Raabe, *Acta Mater.* **131**, 323 (2017).
- [12] Z. Li, F. Körmann, B. Grabowski, J. Neugebauer, and D. Raabe, *Acta Mater.* **136**, 262 (2017).
- [13] Z. Li and D. Raabe, *JOM* **69**, 2099 (2017).
- [14] H. Luo, Z. Li, and D. Raabe, *Sci. Rep.* **7**, 9892 (2017).
- [15] H. Luo, W. Lu, X. Fang, D. Ponge, Z. Li, and D. Raabe, *Mater. Today* **21**, 1003 (2018).
- [16] H. Luo, Z. Li, W. Lu, D. Ponge, and D. Raabe, *Corros. Sci.* **136**, 403 (2018).
- [17] S. Liu, Y. Wu, H. Wang, J. He, J. Liu, C. Chen, X. Liu, H. Wang, and Z. Lu, *Intermetallics* **93**, 269 (2018).
- [18] Z. Li, *Acta Mater.* **164**, 400 (2019).
- [19] S. S. Sohn, A. Kwiatkowski da Silva, Y. Ikeda, F. Körmann, W. Lu, W. S. Choi, B. Gault, D. Ponge, J. Neugebauer, and D. Raabe, *Adv. Mater.* **31**, 1807142 (2019).
- [20] Z. Wu, C. Parish, and H. Bei, *J. Alloys Compd.* **647**, 815 (2015).
- [21] Z. Wang, I. Baker, Z. Cai, S. Chen, J. D. Poplawsky, and W. Guo, *Acta Mater.* **120**, 228 (2016).
- [22] Z. Wang and I. Baker, *Mater. Lett.* **180**, 153 (2016).
- [23] Z. Wang, I. Baker, W. Guo, and J. D. Poplawsky, *Acta Mater.* **126**, 346 (2017).
- [24] J. Chen, Z. Yao, X. Wang, Y. Lu, X. Wang, Y. Liu, and X. Fan, *Mater. Chem. Phys.* **210**, 136 (2018).
- [25] L. Chen, R. Wei, K. Tang, J. Zhang, F. Jiang, L. He, and J. Sun, *Mater. Sci. Eng. A* **716**, 150 (2018).
- [26] Y. Shang, Y. Wu, J. He, X. Zhu, S. Liu, H. Huang, K. An, Y. Chen, S. Jiang, H. Wang, X. Liu, and Z. Lu, *Intermetallics* **106**, 77 (2019).
- [27] M. Wu, Z. Li, B. Gault, P. Munroe, and I. Baker, *Mater. Sci. Eng. A* **748**, 59 (2019).
- [28] R. Wu, A. J. Freeman, and G. B. Olson, *Phys. Rev. B* **53**, 7504 (1996).
- [29] D. E. Jiang and E. A. Carter, *Phys. Rev. B* **67**, 214103 (2003).
- [30] C. Domain, C. S. Becquart, and J. Foct, *Phys. Rev. B* **69**, 144112 (2004).
- [31] J. S. Braithwaite and P. Rez, *Acta Mater.* **53**, 2715 (2005).
- [32] L. Huang, N. V. Skorodumova, A. B. Belonoshko, B. Johansson, and R. Ahuja, *Geophys. Res. Lett.* **32**, L21314 (2005).
- [33] D. E. Jiang and E. A. Carter, *Phys. Rev. B* **71**, 045402 (2005).
- [34] D. W. Boukhvalov, Y. N. Gornostyrev, M. I. Katsnelson, and A. I. Lichtenstein, *Phys. Rev. Lett.* **99**, 247205 (2007).
- [35] B. Hallstedt, D. Djurovic, J. von Appen, R. Dronskowski, A. Dick, F. Körmann, T. Hickel, and J. Neugebauer, *Calphad* **34**, 129 (2010).
- [36] M. Yamaguchi, *Metall. Mater. Trans. A* **42**, 319 (2010).
- [37] A. Abbasi, A. Dick, T. Hickel, and J. Neugebauer, *Acta Mater.* **59**, 3041 (2011).
- [38] A. Dick, F. Körmann, T. Hickel, and J. Neugebauer, *Phys. Rev. B* **84**, 125101 (2011).
- [39] H. Gholizadeh, C. Draxl, and P. Puschnig, *Acta Mater.* **61**, 341 (2013).
- [40] D. J. Hepburn, D. Ferguson, S. Gardner, and G. J. Ackland, *Phys. Rev. B* **88**, 024115 (2013).
- [41] A. V. Ponomareva, Y. N. Gornostyrev, and I. A. Abrikosov, *Phys. Rev. B* **90**, 014439 (2014).
- [42] A. V. Ponomareva, Y. N. Gornostyrev, and I. A. Abrikosov, *J. Exp. Theor. Phys.* **120**, 716 (2015).
- [43] Y. Ikeda and I. Tanaka, *J. Alloys Compd.* **684**, 624 (2016).
- [44] J. Wang, R. Janisch, G. K. Madsen, and R. Drautz, *Acta Mater.* **115**, 259 (2016).
- [45] S. Lu, R. Li, K. Kádas, H. Zhang, Y. Tian, S. K. Kwon, K. Kokko, Q.-M. Hu, S. Hertzman, and L. Vitos, *Acta Mater.* **122**, 72 (2017).

- [46] J. Yang, X. Xing, S. Liu, C. Zhao, Y. Zhao, and Q. Yang, *J. Alloys Compd.* **695**, 2717 (2017).
- [47] D. J. Siegel and J. C. Hamilton, *Phys. Rev. B* **68**, 094105 (2003).
- [48] D. J. Siegel, M. van Schilfhaarde, and J. C. Hamilton, *Phys. Rev. Lett.* **92**, 086101 (2004).
- [49] F. Abild-Pedersen, J. K. Nørskov, J. R. Rostrup-Nielsen, J. Sehested, and S. Helveg, *Phys. Rev. B* **73**, 115419 (2006).
- [50] Y.-A. Zhu, Y.-C. Dai, D. Chen, and W.-K. Yuan, *Carbon* **45**, 21 (2007).
- [51] X. Hu, T. Björkman, H. Lipsanen, L. Sun, and A. V. Krashennnikov, *J. Phys. Chem. Lett.* **6**, 3263 (2015).
- [52] D. D. Stefano, M. Mrovec, and C. Elsässer, *Acta Mater.* **98**, 306 (2015).
- [53] N. I. Medvedeva, D. V. Aken, and J. E. Medvedeva, *J. Phys.: Condens. Matter* **22**, 316002 (2010).
- [54] J. von Appen and R. Dronskowski, *Steel Res. Int.* **82**, 101 (2011).
- [55] N. Medvedeva, M. Park, D. V. Aken, and J. Medvedeva, *J. Alloys Compd.* **582**, 475 (2014).
- [56] T. Hickel, S. Sandlöbes, R. Marceau, A. Dick, I. Bleskov, J. Neugebauer, and D. Raabe, *Acta Mater.* **75**, 147 (2014).
- [57] M. Yao, P. Dey, J.-B. Seol, P. Choi, M. Herbig, R. Marceau, T. Hickel, J. Neugebauer, and D. Raabe, *Acta Mater.* **106**, 229 (2016).
- [58] P. Dey, R. Nazarov, B. Dutta, M. Yao, M. Herbig, M. Friák, T. Hickel, D. Raabe, and J. Neugebauer, *Phys. Rev. B* **95**, 104108 (2017).
- [59] L.-H. Liu, T.-W. Fan, C.-L. Wu, P. Xie, D.-W. Yuan, and J.-H. Chen, *Acta Metall. Sinica* **30**, 272 (2016).
- [60] T. A. Timmerscheidt and R. Dronskowski, *Steel Res. Int.* **88**, 1600292 (2016).
- [61] T. A. Timmerscheidt, P. Dey, D. Bogdanovski, J. Von Appen, T. Hickel, J. Neugebauer, and R. Dronskowski, *Metals* **7**, 264 (2017).
- [62] C. H. Liebscher, M. Yao, P. Dey, M. Lipińska-Chwalek, B. Berkels, B. Gault, T. Hickel, M. Herbig, J. Mayer, J. Neugebauer, D. Raabe, G. Dehm, and C. Scheu, *Phys. Rev. Mater.* **2**, 023804 (2018).
- [63] O. Grässel, L. Krüger, G. Frommeyer, and L. Meyer, *Int. J. Plast.* **16**, 1391 (2000).
- [64] G. Frommeyer, U. Brüx, and P. Neumann, *ISIJ Int.* **43**, 438 (2003).
- [65] D. Pierce, J. Jiménez, J. Bentley, D. Raabe, C. Oskay, and J. Wittig, *Acta Mater.* **68**, 238 (2014).
- [66] O. Bouaziz, S. Allain, C. Scott, P. Cugy, and D. Barbier, *Curr. Opin. Solid State Mater. Sci.* **15**, 141 (2011).
- [67] B. C. D. Cooman, Y. Estrin, and S. K. Kim, *Acta Mater.* **142**, 283 (2018).
- [68] T. Smith, M. Hooshmand, B. Esser, F. Otto, D. McComb, E. George, M. Ghazisaeidi, and M. Mills, *Acta Mater.* **110**, 352 (2016).
- [69] N. L. Okamoto, S. Fujimoto, Y. Kambara, M. Kawamura, Z. M. T. Chen, H. Matsunoshita, K. Tanaka, H. Inui, and E. P. George, *Sci. Rep.* **6**, 35863 (2016).
- [70] J. Liu, C. Chen, Y. Xu, S. Wu, G. Wang, H. Wang, Y. Fang, and L. Meng, *Scr. Mater.* **137**, 9 (2017).
- [71] S. Liu, Y. Wu, H. Wang, W. Lin, Y. Shang, J. Liu, K. An, X. Liu, H. Wang, and Z. Lu, *J. Alloys Compd.* **792**, 444 (2019).
- [72] A. J. Zaddach, C. Niu, C. C. Koch, and D. L. Irving, *JOM* **65**, 1780 (2013).
- [73] S. Huang, W. Li, S. Lu, F. Tian, J. Shen, E. Holmström, and L. Vitos, *Scr. Mater.* **108**, 44 (2015).
- [74] L. Patriarca, A. Ojha, H. Sehitoglu, and Y. Chumlyakov, *Scr. Mater.* **112**, 54 (2016).
- [75] M. Beyramali Kivy and M. Asle Zaeem, *Scr. Mater.* **139**, 83 (2017).
- [76] Z. Zhang, H. Sheng, Z. Wang, B. Gludovatz, Z. Zhang, E. P. George, Q. Yu, S. X. Mao, and R. O. Ritchie, *Nat. Commun.* **8**, 14390 (2017).
- [77] Y. Zhang, Y. Zhuang, A. Hu, J. Kai, and C. Liu, *Scr. Mater.* **130**, 96 (2017).
- [78] S. Zhao, G. M. Stocks, and Y. Zhang, *Acta Mater.* **134**, 334 (2017).
- [79] S. Alkan, A. Ojha, and H. Sehitoglu, *Acta Mater.* **147**, 149 (2018).
- [80] H. Huang, X. Li, Z. Dong, W. Li, S. Huang, D. Meng, X. Lai, T. Liu, S. Zhu, and L. Vitos, *Acta Mater.* **149**, 388 (2018).
- [81] C. Niu, C. R. LaRosa, J. Miao, M. J. Mills, and M. Ghazisaeidi, *Nat. Commun.* **9**, 1363 (2018).
- [82] J. Ding, Q. Yu, M. Asta, and R. O. Ritchie, *Proc. Natl. Acad. Sci. USA* **115**, 8919 (2018).
- [83] Y. Ikeda, F. Körmann, I. Tanaka, and J. Neugebauer, *Entropy* **20**, 655 (2018).
- [84] Y. Ikeda, B. Grabowski, and F. Körmann, *Mater. Charact.* **147**, 464 (2019).
- [85] P. J. H. Denteneer and W. van Haeringen, *J. Phys. C* **20**, L883 (1987).
- [86] K. Momma and F. Izumi, *J. Appl. Crystallogr.* **44**, 1272 (2011).
- [87] A. Zunger, S.-H. Wei, L. G. Ferreira, and J. E. Bernard, *Phys. Rev. Lett.* **65**, 353 (1990).
- [88] T. Bučko, J. Hafner, S. Lebègue, and J. G. Ángyán, *J. Phys. Chem. A* **114**, 11814 (2010).
- [89] H. W. Day, *Am. Mineral.* **97**, 52 (2012).
- [90] Previous computational studies reported that C solution energy at octahedral sites converges into 0.01 eV or less already at the supercell size with 32 lattice atoms for fcc Fe [29,40] and fcc Ni [47]. This indicates that the interaction among C does not substantially affect the C solution energy for C concentrations of less than 3 at. %.
- [91] Since the C occupancies at the interstitial sites in the ideal annealed condition are obtained from a Fermi-Dirac distribution, the procedure to compute $\Delta U_{\text{sol}}(T, x)$ and $\Delta S_{\text{sol}}(T, x)$ from Eqs. (10)–(12) is formally equivalent to the fixed DOS approximation for electronic excitations [84,92–94]. To focus on the contribution per interstitial atom, these quantities are normalized by x in Eqs. (10)–(12).
- [92] C. Wolverton and A. Zunger, *Phys. Rev. B* **52**, 8813 (1995).
- [93] X. Zhang, B. Grabowski, F. Körmann, C. Freysoldt, and J. Neugebauer, *Phys. Rev. B* **95**, 165126 (2017).
- [94] X. Zhang, B. Grabowski, T. Hickel, and J. Neugebauer, *Comput. Mater. Sci.* **148**, 249 (2018).
- [95] Other geometric properties, i.e., surface areas of the interstitial sites and the average distances from the interstitial atoms to the atoms in the INN shells, show very similar trends to those of V_{int} .
- [96] J. M. Sanchez, F. Ducastelle, and D. Gratias, *Physica A (Amsterdam)* **128**, 334 (1984).

- [97] D. de Fontaine, in *Solid State Physics* (Academic Press, New York, 1994), pp. 33–176.
- [98] F. Ducastelle, in *Interatomic Potential and Structural Stability*, edited by K. Terakura and H. Akai (Springer-Verlag, Berlin, 1993), pp. 133–142.
- [99] A. Van der Ven and G. Ceder, *Phys. Rev. B* **71**, 054102 (2005).
- [100] P. E. Blöchl, *Phys. Rev. B* **50**, 17953 (1994).
- [101] J. P. Perdew, K. Burke, and M. Ernzerhof, *Phys. Rev. Lett.* **77**, 3865 (1996).
- [102] G. Kresse, *J. Non-Cryst. Solids* **192–193**, 222 (1995).
- [103] G. Kresse and J. Furthmüller, *Comput. Mater. Sci.* **6**, 15 (1996).
- [104] G. Kresse and D. Joubert, *Phys. Rev. B* **59**, 1758 (1999).
- [105] M. Methfessel and A. T. Paxton, *Phys. Rev. B* **40**, 3616 (1989).
- [106] P. Bhattacharjee, G. Sathiaraj, M. Zaid, J. Gatti, C. Lee, C.-W. Tsai, and J.-W. Yeh, *J. Alloys Compd.* **587**, 544 (2014).
- [107] Z. Wu, Temperature and Alloying Effects on the Mechanical Properties of Equiatomic FCC Solid Solution Alloys, Ph.D. thesis, The University of Tennessee, 2014.
- [108] M. Laurent-Brocq, A. Akhatova, L. Perrière, S. Chebini, X. Sauvage, E. Leroy, and Y. Champion, *Acta Mater.* **88**, 355 (2015).
- [109] B. Schuh, F. Mendez-Martin, B. Völker, E. George, H. Clemens, R. Pippan, and A. Hohenwarter, *Acta Mater.* **96**, 258 (2015).
- [110] C. L. Tracy, S. Park, D. R. Rittman, S. J. Zinkle, H. Bei, M. Lang, R. C. Ewing, and W. L. Mao, *Nat. Commun.* **8**, 15634 (2017).
- [111] F. Zhang, Y. Wu, H. Lou, Z. Zeng, V. B. Prakapenka, E. Greenberg, Y. Ren, J. Yan, J. S. Okasinski, X. Liu, Y. Liu, Q. Zeng, and Z. Lu, *Nat. Commun.* **8**, 15687 (2017).
- [112] D. Ma, B. Grabowski, F. Körmann, J. Neugebauer, and D. Raabe, *Acta Mater.* **100**, 90 (2015).
- [113] K. Jin, B. C. Sales, G. M. Stocks, G. D. Samolyuk, M. Daene, W. J. Weber, Y. Zhang, and H. Bei, *Sci. Rep.* **6**, 20159 (2016).
- [114] F. Körmann, D. Ma, D. D. Belyea, M. S. Lucas, C. W. Miller, B. Grabowski, and M. H. F. Sluiter, *Appl. Phys. Lett.* **107**, 142404 (2015).
- [115] F. Körmann, A. Dick, B. Grabowski, T. Hickel, and J. Neugebauer, *Phys. Rev. B* **85**, 125104 (2012).
- [116] Y. Ikeda, A. Seko, A. Togo, and I. Tanaka, *Phys. Rev. B* **90**, 134106 (2014).
- [117] F. Körmann, B. Grabowski, B. Dutta, T. Hickel, L. Mauger, B. Fultz, and J. Neugebauer, *Phys. Rev. Lett.* **113**, 165503 (2014).
- [118] L. Zhou, F. Körmann, D. Holec, M. Bartosik, B. Grabowski, J. Neugebauer, and P. H. Mayrhofer, *Phys. Rev. B* **90**, 184102 (2014).
- [119] F. Körmann, P.-W. Ma, S. L. Dudarev, and J. Neugebauer, *J. Phys.: Condens. Matter* **28**, 076002 (2016).
- [120] Y. Ikeda, F. Körmann, B. Dutta, A. Carreras, A. Seko, J. Neugebauer, and I. Tanaka, *npj Comput. Mater.* **4**, 7 (2018).
- [121] P. J. Steinhardt, D. R. Nelson, and M. Ronchetti, *Phys. Rev. B* **28**, 784 (1983).
- [122] H. Song, F. Tian, Q.-M. Hu, L. Vitos, Y. Wang, J. Shen, and N. Chen, *Phys. Rev. Mater.* **1**, 023404 (2017).
- [123] F. Körmann and M. H. Sluiter, *Entropy* **18**, 403 (2016).
- [124] H. S. Oh, D. Ma, G. P. Leyson, B. Grabowski, E. S. Park, F. Körmann, and D. Raabe, *Entropy* **18**, 321 (2016).
- [125] N. L. Okamoto, K. Yuge, K. Tanaka, H. Inui, and E. P. George, *AIP Adv.* **6**, 125008 (2016).
- [126] H. S. Oh, S. J. Kim, K. Odbadrakh, W. H. Ryu, K. N. Yoon, S. Mu, F. Körmann, Y. Ikeda, C. C. Tasan, D. Raabe, T. Egami, and E. S. Park, *Nat. Commun.* **10**, 2090 (2019).
- [127] Z. Dong, S. Schönecker, W. Li, D. Chen, and L. Vitos, *Sci. Rep.* **8**, 12211 (2018).
- [128] S. Zhao, Y. Osetsky, G. M. Stocks, and Y. Zhang, *npj Comput. Mater.* **5**, 13 (2019).
- [129] R. G. Hennig, D. R. Trinkle, J. Bouchet, S. G. Srinivasan, R. C. Albers, and J. W. Wilkins, *Nat. Mater.* **4**, 129 (2005).
- [130] R. E. Schramm and R. P. Reed, *Metall. Trans. A* **6**, 1345 (1975).
- [131] As discussed in Ref. [37] in detail, the impact of C atoms on the SFE of pure Fe indeed depends on how the C atoms are distributed. Actually, the solution energy of C atoms in pure Fe was reported to be higher in the vicinity of a stacking fault as compared to the bulk region [37,39,55,59], indicating that, depending on the experimental conditions, C atoms may segregate away from the stacking fault. If C atoms segregate away from the stacking fault, their impact on the actual SFE should become smaller.
- [132] P. Vinet, J. H. Rose, J. Ferrante, and J. R. Smith, *J. Phys.: Condens. Matter* **1**, 1941 (1989).
- [133] A. O. de-la Roza and V. Luaña, *Comput. Phys. Commun.* **182**, 1708 (2011).
- [134] J. Hafner and D. Hobbs, *Phys. Rev. B* **68**, 014408 (2003).
- [135] Y. Mishin, M. Mehl, and D. Papaconstantopoulos, *Acta Mater.* **53**, 4029 (2005).
- [136] S.-L. Shang, Y. Wang, D. Kim, and Z.-K. Liu, *Comput. Mater. Sci.* **47**, 1040 (2010).
- [137] <http://mathworld.wolfram.com/SphericalHarmonic.html>.
- [138] L. Huber, R. Hadian, B. Grabowski, and J. Neugebauer, *npj Comput. Mater.* **4**, 64 (2018).
- [139] D. Scheiber, V. I. Razumovskiy, P. Puschnig, R. Pippan, and L. Romaner, *Acta Mater.* **88**, 180 (2015).
- [140] L. Huber, R. Hadian, and Y. Ikeda, <https://github.com/liamhuber/clustergb>.
- [141] B.-J. Lee and S.-H. Choi, *Modell. Simul. Mater. Sci. Eng.* **12**, 621 (2004).
- [142] A. Togo and I. Tanaka, *Scr. Mater.* **108**, 1 (2015).
- [143] C. Niu, A. J. Zaddach, A. A. Oni, X. Sang, J. W. Hurt III, J. M. LeBeau, C. C. Koch, and D. L. Irving, *Appl. Phys. Lett.* **106**, 161906 (2015).
- [144] T. Fukushima, H. Katayama-Yoshida, K. Sato, M. Ogura, R. Zeller, and P. H. Dederichs, *J. Phys. Soc. Jpn.* **86**, 114704 (2017).
- [145] S. Mu, G. D. Samolyuk, S. Wimmer, M. C. Tropsky, S. N. Khan, S. Mankovsky, H. Ebert, and G. M. Stocks, *npj Comput. Mater.* **5**, 1 (2019).